Holocene dynamics of the southern westerly winds over the Indian Ocean inferred from a peat dust deposition record

Chuxian Li [a, b, *], Jeroen E. Sonke [b], Gaël Le Roux [a], Nathalie Van der Putten [c], Natalia Piotrowska [d], Catherine Jeandel [e], Nadine Mattielli [f], Mathieu Benoit [b], Giles F.S. Wiggs [g], François De Vleeschouwer [a, 1]

[a] EcoLab, Université de Toulouse, CNRS, INPT, UPS, Toulouse, France
[b] Laboratoire Géosciences Environnement Toulouse, Université de Toulouse, CNRS, IRD, UPS, Toulouse, France
[c] Faculty of Science, Earth Sciences, Cluster Earth and Climate, Vrije Universiteit Amsterdam, the Netherlands
[d] Institute of Physics-CSE, Silesian University of Technology, Gliwice, Poland
[e] LEGOS Université de Toulouse, CNRS, CNES, IRD, UPS, Toulouse, France
[f] Laboratoire G-Time, DGES, Université Libre de Bruxelles (ULB), Belgium
[g] School of Geography and the Environment, Oxford University Centre for the Environment, University of Oxford, South Parks Road, Oxford, OX1 3QY, United Kingdom

ARTICLE INFO

ABSTRACT

The southern westerly winds (SWW) play a major role in climate variability in Southern Hemisphere mid- and high-latitudes, regulating rainfall, ocean circulation, and the Southern Ocean carbon sink. Despite their importance, little is known about millennial scale changes in the SWW and how they have influenced the climate system in the past and interacted with the Earth's surface elements, such as dust, nutrients and carbon. Here we present a dust record from a 6.6 kyr old peat core in Amsterdam Island (AMS) situated at the northern edge of the SWW (37°S) in the Southern Indian Ocean. Mineral dust flux was used to track atmospheric dust production, long-distance transport and subsequent deposition. Dust provenance was determined from rare earth element (REE) and Nd isotopic signatures (εNd) in the peat core, compared with a reference dataset of Southern Hemisphere dust sources. Using a multi-proxy mixing model, the εNd and REE ratios show a relatively uniform mixture of ca. 40% local, 15% Southern African and 45% Southern South American dust sources since 6.6 cal kyr BP. However, from 1910 AD onwards, there is a doubling in the contribution from Southern Africa (32%). Two mineral dust flux minima occur at 6.2–4.9 cal kyr BP and 3.9–2.7 cal kyr BP, interpreted as periods with equatorward-shifted and/or strengthened SWW at the northern edge of the wind belt. Conversely, periods of higher dust flux at 6.6–6.2 cal kyr BP, 4.9–3.9 cal kyr BP, and 1.4 cal kyr BP onwards are interpreted as poleward-shifted and/or weakened SWW. These interpretations are based on the findings that higher (lower) wind speeds lead to enhanced (less) removal of distal dust on the way to AMS, by wet deposition and turbulence. Published Holocene SWW records at the northern edge of the wind belt (33–41°S) covering South-America, Southern-Africa and Australia, show much variability over the last 6.6 kyr. We suggest this reflects complex regional climate variability in the different SH longitudinal sectors, indicating that SWW are not zonally homogeneous at the northern edge of the wind belt. The recent shift in dust provenance is not accompanied by enhanced total dust deposition at AMS. We therefore suggest that human impact (e.g., land use changes) and drier climate conditions in Southern Africa have led to enhanced dust mobilization.

© 2020 Elsevier Ltd. All rights reserved.

* Corresponding author. EcoLab / Campus Ensat, Avenue de l'Agrobiopole, 31326, Castanet-Tolosan, France.
E-mail address: chuxian.li@ensat.fr (C. Li).
[1] Present address: Instituto Franco-Argentino para el Estudio del Clima y sus Impactos (UMI 3351 IFAECI/CNRS-CONICET-UBA), Universidad de Buenos Aires, Argentina.

1. Introduction

The strength and position of the southern westerly winds (SWW) vary seasonally due to changes in the sea surface temperature (Lamy et al., 2010). SWW shift equatorward and expand

during the austral winter, while they move poleward and contract during the austral summer. Latitudinal displacement in annual-mean SWW position can be affected by both external factors (e.g., long-term orbital forced insolation changes, Varma et al., 2012, 2011), and internal factors (e.g., Southern Annual Mode changes, Gillett and Thompson, 2003). Changes in the annual-mean strength and position of SWW play a major role in climate variability of Southern Hemisphere (SH) mid- and high latitudes (e.g., affecting precipitation pattern, Jenny et al., 2003). The SWW are also an important driver of ocean circulation, nutrient transport and the global carbon cycle (Kohfeld et al., 2013). Around 40% of anthropogenic CO_2 emissions are currently taken up by the Southern Ocean south of 35°S (Frölicher et al., 2015; Landschützer et al., 2015; Sabine et al., 2004). It has been suggested that poleward-shifts and intensification of the SWW can enhance upwelling of deep water with high concentrations of dissolved inorganic carbon, limiting the capacity of the ocean to absorb carbon at the surface, resulting in additional global warming (Denton et al., 2010; Hodgson and Sime, 2010; Lovenduski et al., 2008).

An increase in SWW strength has been observed in recent decades (e.g., Hande et al., 2012; Marshall et al., 2006; Thompson and Solomon, 2002). Swart and Fyfe, (2012) suggest that under high CO_2 emission scenarios, the SWW could shift up to 1.5° southwards and strengthen by up to 10% by the end of the 21st century (relative to the current annual-mean SWW position and strength). These changes will have significant environmental and climatic implications (Zickfeld et al., 2007). To understand the influence of SWW on Earth's climate requires a better knowledge of the interactions between SWW dynamics and climate in the past, especially in the Holocene (Fletcher and Moreno, 2012).

Up to now, a range of direct and indirect proxies in different stratigraphic archives (e.g., peat and sediment cores) have been used to reconstruct Holocene SWW fluctuations (e.g., Lamy et al., 2010; Moreno et al., 2010; Saunders et al., 2018, 2012; Van der Putten et al., 2008). However, no consensus has been reached on past intensity and/or latitudinal changes of the SWW at the whole wind belt. Some studies argue for a strengthening/equatorward shift of the SWW during the mid-Holocene (ca. 7 - 4 cal kyr BP) relative to the early Holocene (ca. 11 - 7 cal kyr BP) based on studies from Southern Africa (Fitchett et al., 2017; Humphries et al., 2017), Southern South America (Jenny et al., 2003; Moreno et al., 2010), Australia and New Zealand (Shulmeister, 1999). Other studies suggest a poleward displacement of the SWW during the same period resulting in a decreased westerly influence in Southern Africa (Chase et al., 2013), Southern South America (Frugone-Álvarez et al., 2017; Lamy et al., 2010, 2001), Australia and New Zealand (Marx et al., 2011). These studies are mainly conducted on the continents, which are under the combined influence of SWW and other regional climate and orographic factors (e.g., the monsoon system in Australia and the presence of the Andes in South America).

Relatively few paleoclimatic studies (Lindvall et al., 2011; Ljung and Björck, 2007; Saunders et al., 2018, 2012; Van der Putten et al., 2012, 2008), have attempted to reconstruct Holocene SWW variability from oceanic islands where these factors are largely absent. Currently there are no SWW reconstructions at the northern edge of the SWW belt in the southern Indian Ocean. We address this by studying the Holocene mineral dust flux and its composition in peat profiles in Amsterdam Island (37°S). Mineral dust flux is a function of both changes in dust provenance, wind transport and deposition (Vanneste et al., 2015). Specifically, dust flux is a function of environmental factors, including aridity and air mass circulation over source areas (Marx et al., 2009; Thompson et al.,

2002), dust atmospheric residence time (Betzer et al., 1988), as well as the strength and trajectories of transporting winds (Kohfeld et al., 2013). Changes in dust flux can be seen in the variabilities of geochemical and isotopic compositions (e.g., rare earth elements (REE) and Neodymium (Nd) isotopes, Vanneste et al., 2016, 2015). Amsterdam Island is remote and nearly free from human disturbance, which makes it an ideal location to measure dust flux and provenance, and determine past changes in wind dynamics (Gaudichet et al., 1989).

The specific objectives of this study were to: (1) investigate the dust flux in peat core from Amsterdam Island; (2) identify the provenance of the dust by comparing core samples with a reference dataset of dust geochemistry and isotopic signatures from the Southern Hemisphere; (3) interpret these measurements in terms of past changes in the dynamics of the SWW at their northern limit in the Indian ocean, through comparison with other SH records; and (4) probe the anthropogenic impact on the Southern Hemisphere based on the dust variability in Amsterdam Island peat core. This study can also provide an observational dataset for climate model parameterizations, especially in terms of the future impact of changes in the SWW on continental rainfall and the global carbon cycle.

2. Material and methods

2.1. Site description

Amsterdam Island (AMS, 37°50′S, 77°32′E) is a small (55 km²) isolated volcanic island located 4200 km to the east of South Africa and 3200 km to the west of Australia (Fig. 1a and b). The island has steep cliffs along its western coast rising to a central caldera at 720 m above sea level (a.s.l., Flatberg et al., 2011; Doucet et al., 2003, Fig. 1c). The highest point is Mont de La Dives at 881 m a.s.l.. AMS is currently at the northern edge of the SWW belt, and just north of the oceanic subtropical front (Orsi et al., 1995). It has a mild oceanic climate with frequent cloud formation at the caldera. Mean annual temperature at the meteorological station (27 m a.s.l.) is 14 °C and annual precipitation is about 1100 mm (Lebouvier and Frenot, 2007). The wind strength is 7.4 m s^{-1} on average (Météo France data reported in Frenot and Valleix, 1990). However, climate conditions on the central plateau are harsher with a mean annual temperature of 7 °C and twice as much rainfall (Frenot and Valleix, 1990). The soil around the central plateau is poorly developed and consists of water-saturated sandy loams developed to a maximum depth of 60 cm (Frenot and Valleix, 1990). The wetter conditions at higher altitudes of the island (above 500 m a.s.l.) favor moss growth (e.g., *Sphagnum* mosses) and peat accumulation, in particular on the central plateau (Flatberg et al., 2011).

2.2. Sample collection and preparation

A 5 m-long peat sequence (AMS14-PB01A, 37°50.742′S, 77°32.898′E, Fig. 1c) was collected from the center of the caldera peatland at 738 m a.s.l. (Fig. 1; Fig. S1) in December 2014 using a 50 cm long Russian corer with an internal diameter of 10 cm (Belokopytov and Beresnevich, 1955; De Vleeschouwer et al., 2014). Two further cores (AMS14-PB01B, 4.15 m length; AMS14-PB01C, top 1 m length) were collected and archived. Cores were photographed, described, wrapped in plastic film and PVC tubes, and shipped to France refrigerated at +4 °C. Cores were frozen and subsequently sliced at roughly 1-cm resolution using the sub-sampling procedure described in De Vleeschouwer et al. (2010) and Givelet et al. (2004).
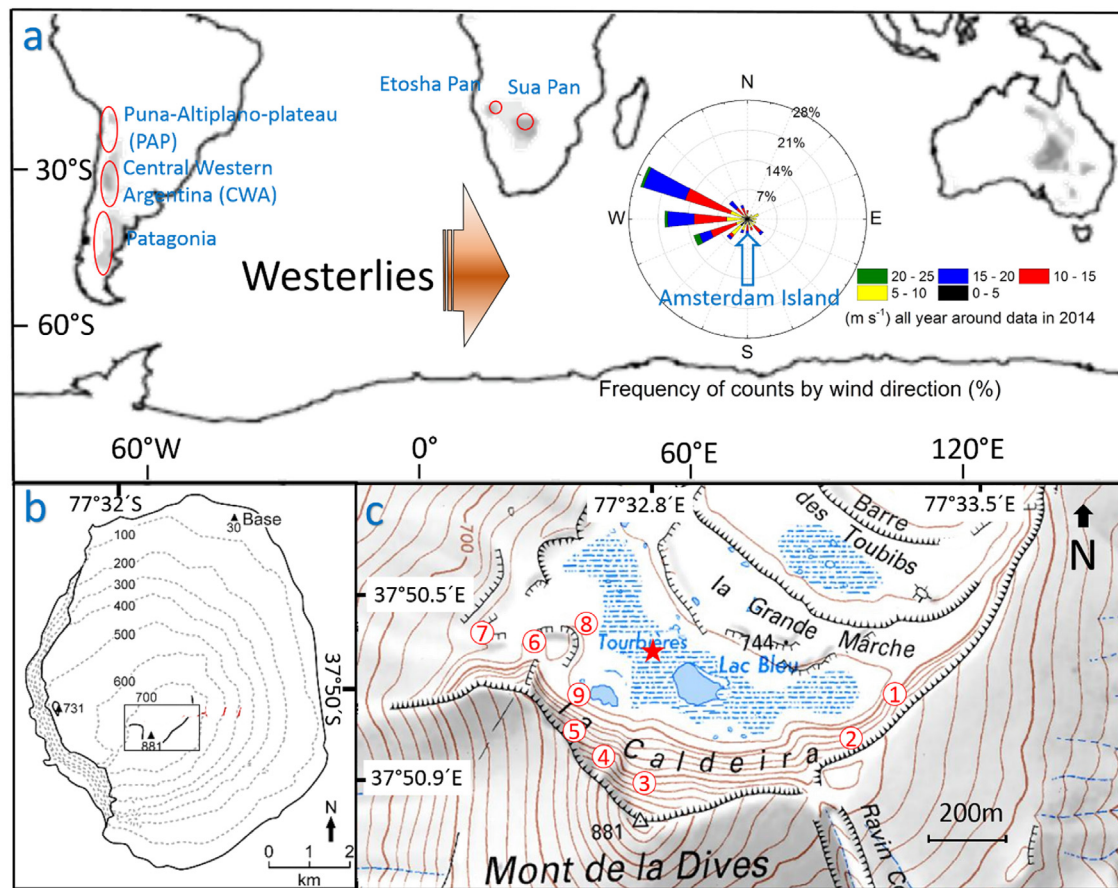
Fig. 1. Sampling sites on Amsterdam Island (AMS) and in the potential dust source areas in the Southern Hemisphere. (a) The core of the wind rose represents the location of Amsterdam Island. Wind rose data are courtesy of the Institut de Géosciences et de l'Environnement in Grenoble, France. The orange arrow represents Southern Westerly winds (SWW), whose core currently centers at 50−55°S (Saunders et al., 2018). The grey areas shown in Southern South America and Southern Africa, represents days per months (darker = more days) with dust activity (modified after Prospero et al., 2002). Red ellipses are soil sampling areas at Puna-Altiplano-Plateau, Central Western Argentina and Patagonia in Southern America (data from Gili et al., 2017); and dust/soil sampling sites at Sua Pan and Etosha Pan in Southern Africa. (b) Map of AMS. The black rectangle has been enlarged in Fig. c. (c) Locations of the peat coring site AMS14-PB01A (red star) and soil sampling sites (numbers shown in red) at AMS. (For interpretation of the references to colour in this figure legend, the reader is referred to the Web version of this article.)

To study the chemical and isotopic provenance of dust in the core, we assembled a reference dataset consisting of nine top soil samples from Amsterdam island, representative of local dust sources (Fig. 1c), together with samples from the two major SH dust sources (Fig. 1a). These were identified from observational and modelling data (Bryant et al., 2007; Engelstaedter and Washington, 2007; Prospero et al., 2002; Vickery et al., 2013) and include: (1) Botswana and Namibia in Southern Africa; and (2) the Altiplano, Western Argentina and Patagonia in Southern South America. Australia is not considered as an important distal dust source for AMS because limited air masses originate from Australia according to the 14-day Hysplit back trajectory ensembles at AMS (Fig. S2, Text S1) and most Australian dust is transported eastward to the Pacific Ocean (Li et al., 2008). Chemical analysis on AMS also supports minimal present Australian dust contribution to AMS (Gaudichet et al., 1989). Specific reference dust/soil samples in this study were collected from (1) local; (2) Sua Pan (Botswana) and (3) Etosha Pan (Namibia) in Southern Africa (Fig. 1a, c). More information on Southern African dust/soil and local AMS soil are given in the supplementary information Text S2, Table S1 and Table S2, respectively. The dataset of Southern American surface sediments (including Puna-Altiplano-Plateau, Central Western Argentina and Patagonia) are from Gili et al. (2017).

2.3. Analyses and methods

2.3.1. Radiocarbon dating and age model construction

Twenty peat samples were submitted for radiocarbon dating. Where possible monospecific terrestrial plant remains (brown mosses or *Sphagnum* mosses) were dated, and where there was insufficient material, both taxa were combined. Eleven of the radiocarbon samples were pre-treated and graphitized at the GADAM center (Gliwice, Poland, GdA code) (Piotrowska, 2013) and their ^{14}C concentration in graphite measured at the DirectAMS Laboratory (Bothell, WA, USA). The NIST Oxalic Acid II standard was used for normalization, and black coal was used as a blank. The other nine radiocarbon samples were pre-treated, graphitized and dated at Plateforme Nationale LMC14 (CNRS-CEA Saclay, France, SacA code). Normalization of the measurements at LMC14 Laboratory was done with Oxalic Acid 1 standard. Blanks were carbonate and charcoal (for details see Delqué-Količ et al., 2013; Moreau et al., 2013).

The surface of the core was dated with ^{210}Pb using the Constant Rate Supply model (Appleby, 2001), together with four post-bomb radiocarbon dates (Goodsite et al., 2001; Hua, 2009). The ^{210}Pb Constant Rate Supply model has been validated by ^{137}Cs and ^{241}Am measurements (see Li et al., 2017 for details). An age-depth model

was generated from a combination of radiocarbon dating, post-bomb and ^{210}Pb dating with the Bacon package version 2.2 updated in 2018 (Blaauw and Christen, 2011) within R software version 3.5 (R Development Core Team, 2013) using the SHCal13 calibration curve (Hogg et al., 2013). For modelling, the core was divided into 101 sections. The prior settings were default 10 year/cm for accumulation rate (gamma distribution with shape 1.5), and memory was described by beta distribution with mem.strength = 4 and mem.mean = 0.7. The median modelled age was used for plotting the data against time.

2.3.2. Bulk density and ash content

The density (g m^{-3}) of 377 samples was obtained by measuring the volume of each sample, using a Vernier caliper, and weighing it after freeze-drying using an ALPHA 1e4 LD plus freeze-dryer. The ash content was determined as the weight difference before and after ashing the bulk peat samples in a furnace at 550 °C for 5 h.

2.3.3. Major and trace element analyses

We selected 101 freeze-dried AMS peat samples for elemental analysis based on the bulk density results. 100 mg of each selected peat samples was used and 50 mg of each reference soil/dust samples was used. These samples were digested in Teflon vials on a hot plate using an HNO$_3$–HF mixture (method modified from Vanneste et al., 2015, see Supplementary Information Table S3 for more details). Subsequently, concentrations of Al, Ti, K and Sr were determined by ICP-OES (IRIS Intrepid II) at Ecolab (Toulouse, France). Concentrations of trace elements (REE, Ga, Hf, Zr, Th, U, Cs, Rb, Pb), Mg and Ca were measured by quadrupole ICP-MS (Agilent Technologies 7500ce) at the Observatoire Midi-Pyrénées (Toulouse, France).

Synthetic multi-element calibration solutions were used to calibrate the ICP-OES and ICP-MS instruments. In addition, In–Re was added to both the ICP-MS calibration solutions and samples as an internal standard. Several certified reference materials (CRMs) were used for quality control: (1) NJV942 (Sphagnum peat, Swedish University of Agricultural Sciences, Sweden); (2) NJV941 (Carex peat, Swedish University of Agricultural Sciences, Sweden); (3) SRM1515 (Apple leaves, NIST, US); (4) SRM1547 (Peach leaves, NIST, US); (5) LKSD-3 (lake sediment, CANMET Mining and Mineral Sciences Laboratories, Canada); and (6) WQB-1 (lake sediment, National Water Research Institute, USA). For further details on the quality control and quality assurance see supplementary information Text S3, Table S4 and Table S4bis.

2.3.4. Neodymium isotope analyses

43 freeze-dried samples from the AMS peat core, and reference soil samples from AMS (nine samples), Sua Pan (three soil and three dust samples), and Etosha Pan (three soil and three dust samples), were selected for Nd isotope analysis. The weight of the peat samples (160 mg–950 mg) and soil/dust samples (68 mg–275 mg) required for the analyses was based on their Nd concentrations and the sensitivity of the mass spectrometer. Before being digested in a mixture of concentrated HNO$_3$ and HF, samples were ashed in a furnace at 550 °C for 5 h (Vanneste et al., 2015). Subsequently, Nd was separated from the matrix within the sample solution using a two-column ion exchange technique. The Nd isotope composition of all the samples was determined by Thermal Ionization Mass Spectrometry (TRITON™ Plus) at the Observatoire Midi-Pyrénées (Toulouse, France). Chemical blanks for Nd isotopic measurements were below the detection limit. The Nd standards Rennes (^{143}Nd/^{144}Nd = 0.511,973) and La Jolla (^{143}Nd/^{144}Nd = 0.511,858) were analyzed at every session to monitor instrumental drift. Measured values of La Jolla were 0.511,844 ± 0.000012 (n = 9) and

of Rennes were 0.511,956 ± 0.000006 (n = 22). The three replicated samples gave consistent ^{143}Nd/^{144}Nd values within the error bars.

The Nd isotopic signatures, expressed in ϵNd notation are calculated by the equation (1).

$$\epsilon Nd = \left(\frac{\left(\frac{143_{Nd}}{144_{Nd}}\right)\text{Sample}}{\left(\frac{143_{Nd}}{144_{Nd}}\right)CHUR} - 1 \right) \times 10^4 \tag{1}$$

where CHUR is Chondritic Uniform Reservoir, representing a present day average earth value (^{143}Nd/^{144}Nd)$_{CHUR}$ = 0.512,638 (Jacobsen and Wasserburg, 1980). ϵNd represents the deviation of ^{143}Nd/^{144}Nd in a sample from the value in CHUR.

2.4. Statistical methods

A principal component analysis (PCA) was performed on all the elemental data (REE, Mg, Ca, Ga, Rb, Zr, Cs, Hf, Th, U, Al, Pb, Ti, K, Sr) using the 'psych' package (Revelle, 2019) within R software (R Decelopment Core Team, 2013). Each principal component groups a set of elements with similar variations along the peat profile. A varimax rotation is also performed for maximizing the variances of the squared loadings in the components in order to facilitate the interpretation (Abdi and Williams, 2010; Vanneste et al., 2016).

Change point analysis was performed with the Change-Point Analyzer 2.0 software (Taylor Enterprises Inc., IL, http://www.variation.com) to identify significant shifts in the key proxies through the Holocene (e.g., Castino et al., 2016; Killick et al., 2010; Reid et al., 2016). The method (Taylor, 2000a) is based on the mean-shift model under the procedure of a combination of time-series cumulative sum charts and bootstrapping to detect change. The "cumulative sum" mean the cumulative sum of the differences between the values and the average (for details on the method see Taylor, 2000a, 2000b). The cumulative sum chart is optimal at detecting shifts in the mean (Taylor, 2000a). 10,000 bootstraps were performed and only changes with probabilities of >99% were considered.

2.5. Source end-members mixing calculation

The potential distal dust sources are discussed at a continental scale (e.g., Southern South America and Southern Africa) because our initial mixing model attempts have shown that the sources cannot be resolved on a sub-continental scale. Puna-Altiplano-Plateau, Central Western Argentina and Patagonia were grouped together as the Southern South American dust source end-member. Sua Pan and Etosha Pan were grouped as the Southern African end-member. The contributions of different source end-members were calculated based on the method of ratio-to-ratio relationships in the mixing balance described in Albarède (1996) as equation (2):

$$\left(\frac{C^{i2}}{C^{i1}}\right)_{mix} = \frac{\sum_{j=1}^{n} C_j^{i2} f_j}{C_{mix}^{i1}} \tag{2}$$

Where C^{i1} and C^{i2} are the REE concentrations or Nd isotopes in a mixture of n components j and represents each component (end-member). f is the fraction of component j in the mixed dust depositing at AMS. Details on the calculation are reported in Table S5.

3. Results

3.1. Core description

The total length of the core is 500 cm. Between 500 cm and 340 cm depth, a compacted, in general relatively well-preserved peat deposit was formed. The peat is laminated, showing a cm-scale alternation between fibrous well preserved *Sphagnum*-dominated layers and more amorphous less well preserved layers. From 340 cm to 20 cm the peat becomes less compacted showing different units of more or less well preserved peat, with visible plant macrofossils in some parts. The top 20 cm of the core reflects the modern vegetation which consists mainly of brown mosses together with some *Sphagnum* spp. (Fig. S3)

3.2. Bulk density and ash content

The density profile of the AMS peat core shows a general decreasing trend with an abrupt drop at ~315 cm (Fig. 2a). From 500 cm to 315 cm, the median density is 0.17 g cm^{-3} (0.08−0.26 g cm^{-3}) with relatively higher values between 340 cm and 315 cm. From 315 cm upwards, the density is lower with a median value of 0.12 g cm^{-3} (0.05−0.16 g cm^{-3}). The ash content in the AMS peat core mirrors partly the density profile and shows a general decreasing trend from bottom to top (Fig. 2b), varying between 2.63% and 0.34%. The abrupt decrease between 340 cm and 315 cm present in the density profile is not present in the ash content.

3.3. Geochronology

Radiocarbon and calibrated ages are shown in Table 1. The ^{210}Pb,

^{137}Cs and ^{241}Am results are published in Li et al. (2017). The ^{210}Pb Constant Rate Supply model is in good agreement with post-bomb ^{14}C ages. The age-depth model of the core was based on a combination of radiocarbon dating, post-bomb and ^{210}Pb dating (Fig. 2c; Fig. S4). The model shows that the peat sequence spans the last 6.6 kyr (Table S6), with a mean accumulation rate of 0.76 mm yr^{-1}.

3.4. Peat REE and Nd isotopic signatures

The concentration of the entire REE suite varies between 0.18 and 1.26 µg g^{-1} (Table S7). The variations in the down core concentrations of fourteen REE elements (La, Ce, Pr, Nd, Sm, Eu, Gd, Tb, Dy, Ho, Er, Tm, Yb and Lu) are similar to each other. The Nd concentration profile is plotted as an example (Fig. 3a). The ϵNd signature at the bottom of the peat core is −0.8 ± 0.2 (2σ, n = 1). There is a general decreasing trend in ϵNd values between 6.6 and 5.4 cal kyr BP, followed by an approximately three-fold increase at 4.4−3.9 cal kyr BP. The lowest ϵNd values occur at 3.3−2.7 cal kyr BP, after which the ϵNd fluctuates with an overall increasing trend since 2.7 cal kyr BP. The Holocene peat ϵNd profile is relatively constant centering at −2 ± 1.2 (1σ, n = 34, Fig. 3b, Table S7), except for the last 100 years showing more distinct negative signatures with an average value of −7 ± 1.5 (1σ, n = 7).

REE ratios can be used for dust provenance-tracing. The Eu anomaly (Eu/Eu*) was calculated with the equation Eu/Eu* = [Eu]/(([Sm]+[Gd])/2). The ratios of La/Yb and Eu/La have been normalized to Upper Continental Crust (Wedepohl, 1995). Peat average Eu/Eu*, La/Yb$_N$ and Eu/La$_N$ values since the last 6.6 kyr are 1.03 ± 0.10, 0.50 ± 0.07 and 2.01 ± 0.30 (1σ, n = 101), respectively. The signatures of peat Eu/Eu*, La/Yb$_N$ and Eu/La$_N$ remain relatively constant during the last 6.6 kyr (Fig. 3c, d, e), except for the last 100 years, which are characterized by an overall decreasing trend in Eu/Eu*
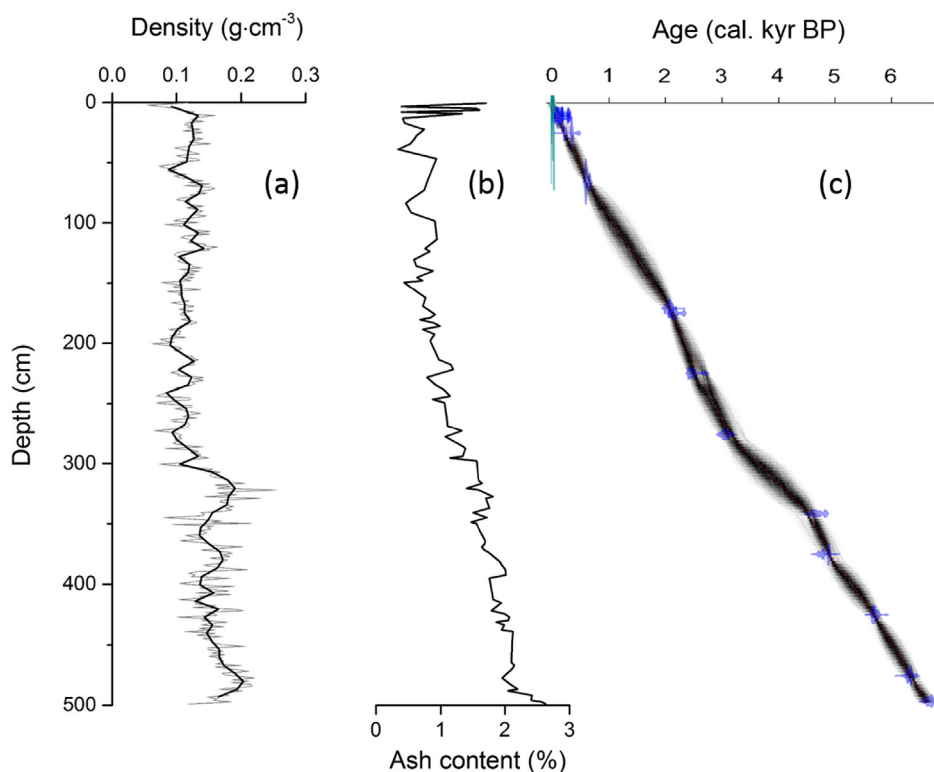

Fig. 2. (a) Density (black line = for 5-point smoothing), (b) ash content and (c) age depth model (^{14}C in blue, ^{210}Pb Constant-Rate-Supply model in green) of the AMS peat core. For details on the top 50 cm chronology, we refer to Fig. S4 in supplementary information. (For interpretation of the references to colour in this figure legend, the reader is referred to the Web version of this article.)

Table 1
Radiocarbon dating results from Amsterdam Island peat sequence. Four samples were dated to a post-bomb period (Goodsite et al., 2001; Hua, 2009; Spalding et al., 2005) and the results calibrated using SH zone 1−2 calibration curve (Hua et al., 2013) by Calibomb software of Queen's university, Belfast. Other results were calibrated using the SHCal13 calibration curve (Hogg et al., 2013). Age-depth modelling was performed with Bacon, R routine (Blaauw and Christen, 2011).

Lab ID	Mid-Point Depth (cm)	Material dated	Radiocarbon age BP / pMC[a]	Calibrated age (median)	Calibrated age with 95.4% probability (BP)
SacA50049	2.0	*Chorisondontium/Dicranoloma* stems + leaves	107.18 ± 0.28 pMC		[-58; −53]
SacA50050	3.5	Brown moss stems	120.36 ± 0.30 pMC		[-37; −35]
SacA50051	4.9	Brown moss + liverworts stems	146.21 ± 0.32 pMC		[-24; −22]
SacA50052	6.4	Brown moss + liverworts stems	116.81 ± 0.28 pMC		[-10; −10]
SacA50053	7.8	Brown moss stems	135 ± 30	8	1−16
SacA50054	9.4	Brown moss stems	115 ± 30	26	14−39
SacA50055	10.8	Brown moss stems + leaves	80 ± 30	44	27−62
SacA50056	12.0	Brown moss stems + *Chorisondontium/Dicranoloma* leaves	160 ± 30	57	33−96
SacA50057	13.2	Brown moss stems	70 ± 30	65	35−127
GdA-4136	24.9	brown moss stems	275 ± 25	198	150−310
GdA-4558	65.4	Residue (*Sphagnum* dominated)	595 ± 25	561	510−640
GdA-4560	170.7	Brown moss stems	2100 ± 25	2028	1920−2105
GdA-4137	174.8	Brown moss stems	2170 ± 30	2076	2005−2145
GdA-4138	224.4	Brown moss stems	2430 ± 30	2530	2365−2700
GdA-4139	275.4	Brown moss stems	2925 ± 30	3092	2930−3330
GdA-4561	340.9	Brown moss stems	4145 ± 35	4485	4225−4645
GdA-4140	374.4	*Sphagnum*	4285 ± 30	4850	4700−5025
GdA-4141	424.4	*Sphagnum* + brown moss	4960 ± 30	5630	5500−5745
GdA-4142	474.8	*Sphagnum* stems	5515 ± 35	6280	6140−6410
GdA-4143	495.9	*Sphagnum* stems	5860 ± 35	6565	6420−6700

[a] pMC is percent modern carbon
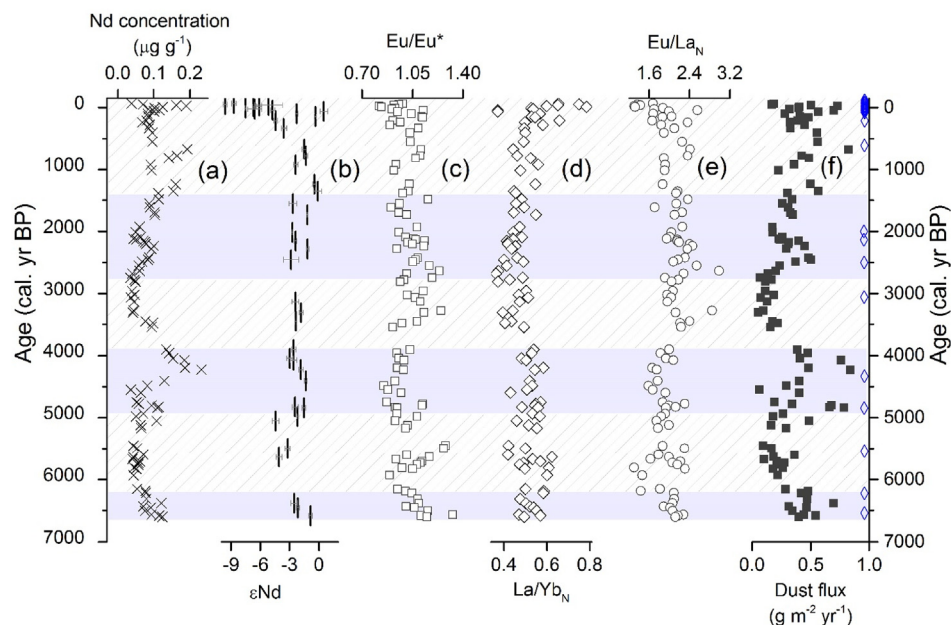
Fig. 3. Profiles of (a) Nd concentration (μg g^{-1}); (b) Epsilon Neodymium (εNd); (c) Eu/Eu*; (d) La/Yb$_N$; (e) Eu/La$_N$; and (f) REE−based dust flux (g m^{-2} yr^{-1}) in AMS peat core. Diamonds represent the ^{14}C dated peat layers (20 in total). The blue and white shading are the zones determined by change point analysis for AMS dust flux. (For interpretation of the references to colour in this figure legend, the reader is referred to the Web version of this article.)

and Eu/La$_N$ ratios, and an increasing trend in La/Yb$_N$ ratio.

4. Discussion

4.1. Elemental proxy interpretation

The results of the PCA are reported in Fig. 4a and Fig. S5. The first component (PC1), explains 70% of the total variance and consists of the entire REE suite and Ga, U, Th, Hf, Zr, Ti, Al (Fig. 4b and c), which are known to be immobile and conservative elements. The second component (PC2), accounts for 14% of the total variance and consists of K, Rb, Pb, and Cs (Fig. 4d and e). The variability of this component is mainly driven by changes in the top part of the core, caused by biological uptake and recycling by the surface moss vegetation (principally K, Rb and, to a lesser extent Cs based on Fig. 4a) as well as anthropogenic Pb deposition (Damman, 1978; Shotyk, 1997). The third component (PC3), explains 12% of the total variance, and includes Sr, Ca and Mg (Fig. 4f and g), which show higher values towards the bottom of the core (Shotyk, 1997).
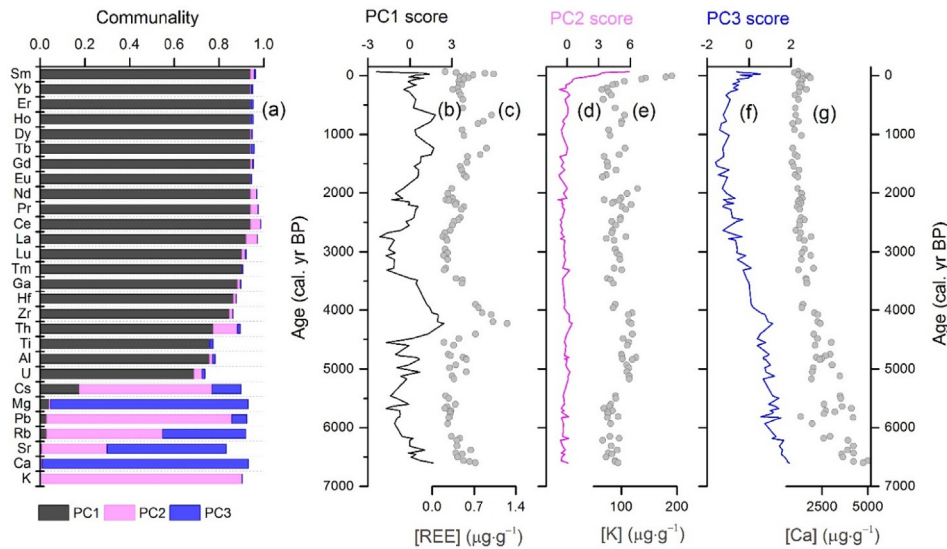
Fig. 4. (a) Relative importance of each principal component (PC) for each chemical element (b−g) PC scores (i.e. transformed variable values for each sample); and their respective representative elements. All the representative elements are shown as concentration (μg g^{-1}).

4.2. Dust deposition

The REE, also reflected by PC1, represent immobile and conservative elements. Therefore, the mineral deposition rate (dust flux, g m^2 yr^{-1}) was calculated as equation (3):

$$\text{Dust flux}_i = \frac{\sum [REE]_i \times peat\ vertical\ AR_i \times density_i}{\sum [REE]_{UCC}} \times 10000$$

(3)

Where $\sum [REE]_i$ is the sum of all REE concentrations (μg g^{-1}) in sample i, *peat vertical AR$_i$* is the peat accumulation rate (cm yr^{-1}), obtained by *depth length$_i$/age interval$_i$*), *density$_i$* is the density of the sample (g cm^{-3}), $\sum [REE]_{UCC}$ is the sum of the REE concentrations in the upper continental crust (Wedepohl, 1995).

The dust flux profile shown in Fig. 3, varies from 0.05 to 0.84 g m^2 yr^{-1} with a median value of 0.32 g m^2 yr^{-1} (Fig. 3f). The REE-based AMS dust flux is comparable to the late Holocene ^{232}Th reconstructed dust flux of 0.5−1.0 g m^{-2} yr^{-1} over the Western Indian Ocean (Kienast et al., 2016). Individual dust flux values are sensitive to spikes in REE concentration, to the age model, and to the peat density. The highest dust fluxes are recorded at ca. 4.2 cal kyr BP and ca. 4.8 cal kyr BP, and are related to maxima in REE concentration and peat accumulation rate. We applied a change-point analysis to identify changes in the probability distribution of the dust flux. Four change-points with >99% confidence level, were identified: 6.2 cal kyr BP; 4.9 cal kyr BP; 3.9 cal kyr BP; 2.7 cal kyr BP and 1.4 cal kyr BP. We therefore separate the dust flux profile into six zones for discussion (see blue and white shading on Fig. 3, and section 4.4): (1) 6.6−6.2 cal kyr BP; (2) 6.2−4.9 cal kyr BP; (3) 4.9−3.9 cal kyr BP; (4) 3.9−2.7 cal kyr BP; (5) 2.7−1.4 cal kyr BP; (6) 1.4 cal kyr BP to the present (2014 AD).

The median ash content of 1.3% (n = 101) in AMS peat core is low compared to the one of 2.9% recorded in a peat core from Tierra del Fuego in Southern South America (Vanneste et al., 2016) and 12.9% from a core in the Mfabeni peatland in Southern Africa (Humphries et al., 2017). The low ash content suggests limited groundwater inputs, even in the deeper minerotrophic part of the bog (detailed explanations for trophic status see Supplementary Information Text S4 and Fig. S6).

4.3. Dust provenance

Studies on atmospheric deposition at AMS, using ^{222}Rn, ^{210}Pb and air mass back trajectories suggested some continental inputs to AMS, in particular from Southern Africa (Angot et al., 2014; Gaudichet et al., 1989; Polian et al., 1986), and Southern South America (Fig. S2). Comparison of εNd values in the AMS peat sequence with the reference datasets of the potential dust source end-members (local, Southern Africa, and Southern South America) show that εNd values of the peat samples lie between the local and continental dust sources (Fig. 5, Fig. S7). This also suggests that AMS can potentially receive dust from local, Southern African, and Southern South American sources.

The AMS soil samples display slightly higher Eu/Eu* (median 1.24, Fig. 5) and lower La/Yb$_N$ ratios (median 0.27, Fig. 5) compared to the peat samples. The Southern African end-member (including both Sua Pan and Etosha Pan) has Eu/Eu* ratios that are close to those for the AMS peat samples, but show higher La/Yb$_N$ ratios (median 1.04). In comparison with the peat samples, Eu/Eu* ratios are relatively lower and La/Yb$_N$ ratios are analogous in the Southern American end-member (including Puna-Altiplano-Plateau, Central Western Argentina and Patagonia, Gili et al., 2017). The average εNd value of the AMS soil samples is 3.9 ± 0.2 (2σ, n = 7, Fig. 5b), much higher than those in the peat samples (εNd −9.6 - 0.5). The Southern African end-member has a more negative signature of −24 ± 1.7 (1σ, n = 11, Fig. 5b). Both εNd (median 3.84) and Eu/La$_N$ (median 3.52) are higher in the local soils than in the Southern African end-member (median εNd = −24.72, median Eu/La$_N$ = 1.44). The εNd signatures in the Southern South American end-member overlap with those in the peat samples, while the Eu/La$_N$ ratios are relatively lower in the Southern South American end-member.

Using the multi-proxy mixing model (Fig. 5), εNd and REE ratios indicate that the peat received approximately 40% of dust from local sources, 15% from Southern Africa and 45% from Southern South America. Dust source proportions were relatively constant over the last 6.6 kyr, except during the last 100 years (Table 2). Since 1910 AD, the model estimates a relative decrease in the local dust input (15%), while the relative contribution of Southern South Africa doubled (32%), with the Southern South American dust
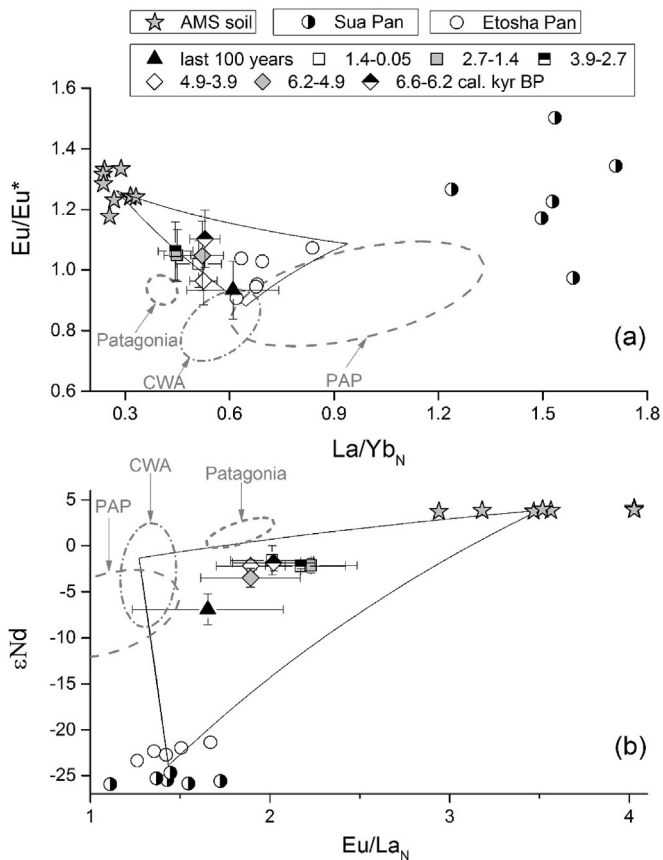
Fig. 5. Relationships of La/Yb$_N$ vs Eu/Eu* (a), and Eu/La$_N$ vs ϵNd (b) in AMS peat together with its Potential Source Areas (normalized to UCC, Wedepohl, 1995). Peat samples are shown in triangles/squares/diamonds, with different shapes representing different periods, such as the last 100 years (number of samples based on Fig. 5a, n = 8), 1.4−0.05 cal kyr BP (n = 17), 2.7−1.4 cal kyr BP (n = 21), 3.9−2.7 cal kyr BP (n = 13), 4.9−3.9 cal kyr BP (n = 15), 6.2−4.9 cal kyr BP (n = 17), and 6.6−6.2 cal kyr BP (n = 10), respectively. Black-edge stars: AMS soils; Half-open circles: dust/soil in Sua Pan; Open circles: dust/soil in Etosha Pan. Puna-Altiplano-Plateau (PAP, nine data points), Central Western Argentina (CWA, five data points) and Patagonia (11 data points) are shown in Elipses (mean data with 95% confidence level, Gili et al., 2017); The black lines in (a) and (b) represent the End-member mixing lines among AMS soil, Southern Africa (Sua Pan + Etosha Pan) and Southern South America (PAP + CWA + Patagonia) (see Supplementary Information Table S5 for detailed calculations, after Albarède, 1996).

component (53%) showing little significant change.

In addition to an important local dust contribution (40%), likely from weathered basalt cliffs adjacent to the AMS peat bog, the mixing model indicates that from 6.6 cal kyr BP to 1910 AD, Southern South America is an important contributor of dust (45%; Table 2). The 14-day back trajectories show the air masses passing AMS that partially originate from Southern South America,

covering the Puna-Altiplano-Plateau, Central Western Argentina and Patagonia (Fig. S2). This is also supported by modern dust observations. For example, combining ground/satellite observations and atmospheric modelling, Gaiero et al. (2013) found that large dust storms at the Puna-Altiplano-Plateau (15° and 26°S) can be developed and injected into the high-altitude subtropical jet stream of the SWW, which hence can be transported over long distances (Gaiero, 2007). Dust from the Central Western Argentinean lowlands (between ~27° and ~39°S), can also be uplifted by strong vertical air motion and be entrained into the SWW (Gili et al., 2017). Once lifted into the troposphere, dust can be transported over thousands of kilometers from its source area (Mahowald et al., 2005). Johnson et al. (2011) have shown that Patagonian dust travels along the SWW pathways to the Southern Indian Ocean during dust outbreak events in the austral summer, potentially reaching the Southern Indian Ocean in a short period of time (days).

The mixing model also confirms a small (9−15%) but significant proportion of Southern African dust through most of the Holocene (Table 2; Fig. 6). The Makgadikgadi Basin in Botswana represented by our Sua Pan samples is the principal persistent dust source in Southern Africa, with a general maximum dust emission activity in August−October (Prospero et al., 2002). The prevailing winds in the area of Sua Pan (Fig. 1a) are tropical Easterlies that bring moisture from the Indian Ocean (Bryant et al., 2007). Etosha Pan situated in the semi-north of Namibia is a second principal Southern African dust source with prevailing northeasterly winds (Vickery et al., 2013; Von Holdt et al., 2017). Both Sua Pan and Etosha Pan are characterized by a proportion of northwesterly winds (Piketh, 2002; Von Holdt et al., 2017), confirming that dust from Sua Pan and Etosha pan can be transported eastward into the Indian Ocean (Fig. S2).

4.4. Lower dust input under equatorward-shifted/strengthened SWW

The dust provenance mixing model showed that the relative proportion of dust contributions from local, Southern African and Southern South American sources remained more or less constant over the mid-to late Holocene at AMS. The estimated dust deposition flux (g m^{-2} yr^{-1}), however, varied substantially on millennial timescales (Fig. 3a), likely resulting from changes in the position and/or intensity of SWW. It is important to realize that a northward shift in SWW may result in multiple antagonistic effects on dust: in dust source areas, an increase in SWW strength may mobilize more dust. However, stronger SWW are characterized by more humid conditions and more rainfall at least at the western to central sectors of the regions, leading to denser vegetation and soil dust immobilization. Additionally, in the case of the high altitude Puna-Altiplano-Plateau and Sua Pan/Etosha Pan, the dust source areas do not directly lie within the SWW belts, but their dust mobilizations can be influenced by SWW (see section 4.2). The net effect of

Table 2
The mean dust contributions of local, Southern African and Southern American dust to the AMS peat sampling site from mid to late Holocene. Estimates are based on a REE proxy mass balance model. Potential African and South American dust sources are lumped (see text). Uncertainty range corresponds to 1σ.

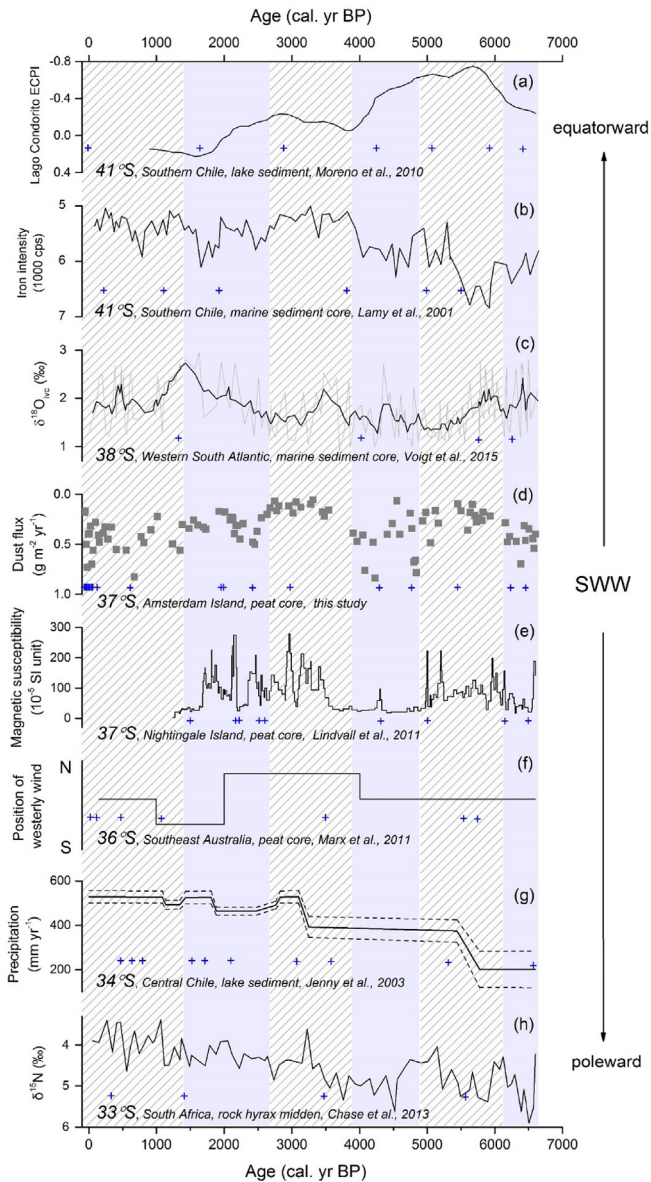| Time interval (cal kyr BP)	local	Southern Africa	Southern America
the last 100 years	15% (5%−25%)	32% (25%−40%)	53% (40%−65%)
1.4−0.05	41% (35%−50%)	15% (10%−20%)	44% (30%−55%)
2.7−1.4	44% (35%−55%)	12% (5%−20%)	44% (30%−55%)
3.9−2.7	46% (40%−55%)	15% (10%−20%)	39% (25%−50%)
4.9−3.9	36% (30%−40%)	9% (5%−15%)	55% (40%−70%)
6.2−4.9	35% (25%−40%)	15% (5%−25%)	50% (35%−70%)
6.6−6.2	41% (35%−45%)	9% (5%−15%)	50% (45%−60%)

Fig. 6. Proxy records for wind position/strength at the northern SWW margin. (a) Pollen index *Eucryphia + Caldcluvia/podocarps* (ECPI) from lake sediment core at Lago Condorito from Southern Chile (Moreno et al., 2010); (b) Iron intensity from marine core GeoB 3313−1 in Southern Chile (Lamy et al., 2001); (c) Ice volume corrected *Globorotalia inflata* $\delta^{18}O$ ($\delta^{18}O_{ivc}$) from marine sediment GeoB13862-1 in Western South Atlantic (Voigt et al., 2015). Black line represents for the 5-point smoothing; (d) AMS mineral dust deposition from this study; (e) Magnetic susceptibility from a peat core in Nightingale Island, Southern Atlantic (Lindvall et al., 2011); (f) Shift in the position of SWW described in Marx et al. (2011); (g) Precipitation reconstruction from Lake Aculeo in Central Chile (Jenny et al., 2003); (h) $\delta^{15}N$-derived humidity from the hyrax middens Seweeekspoort-1-5 in South Africa (Chase et al., 2013). The blue and white shading are the zones determined by change point analysis for AMS dust flux. Crosses indicate ^{14}C dates. (For interpretation of the references to colour in this figure legend, the reader is referred to the Web version of this article.)

stronger SWW on dust emission therefore depends on local geography, meteorology and vegetation (Marx et al., 2018). Studies on climate variability in AMS dust source areas indicate enhanced dryness (e.g., relative higher dust availability) during 6.2−4.9 cal kyr BP and 3.9−2.7 cal kyr BP in both Puna-Altiplano-Plateau (Pueyo et al., 2011) and Southern Africa (Chase et al., 2017; Chevalier and Chase, 2015; Cohen and Tyson, 1995; Cordova et al., 2017; Nash et al., 2006). Dust mobilization in these

source areas should therefore have been constant or possibly enhanced during these two periods.

During periods of equatorward shifted and/or strengthened SWW potentially enhanced dust mobilization will be subjected to more intense removal by rainfall and by turbulence via dry deposition during transport (Miller et al., 1993; Moody et al., 1991). Evidence for this is based on the relationship between rainfall chemistry and seasonal and inter-annual large-scale atmospheric circulation patterns at AMS (Moody et al., 1991). Observed minima in rainfall anion concentrations (non-sea salt Cl and SO_4, from continental origin) during austral winters, characterized by stronger winds and enhanced precipitation. Distal dust records such as AMS, thousands of kilometers away from dust sources, will overall tend to register decreased distal dust deposition during stronger and/or equatorward shifted SWW due to the dominant effect of dust removal during transport (Li et al., 2008). Stronger SWW with higher precipitation can decrease local dust mobility by increasing humidity and possbily local vegetation cover. We therefore suggest that the AMS mineral dust flux minima from 6.2 to 4.9 cal kyr BP and 3.9−2.7 cal kyr BP represent periods of equatorward shifted and/or strengthened SWW at this northern edge with higher wind speed and enhanced precipitation over the dust transport trajectories, regardless of the potential enhanced dust mobility at the source areas during these two periods. Conversely, the three episodes of higher dust inputs (6.6−6.2 cal kyr BP; 4.9−3.9 cal kyr BP; 1.4 cal kyr BP to present) represent periods of poleward-shifted and/or weakened SWW accompanied by overall lower wind speeds and lower precipitation along the air mass trajectories from the Southern Africa and Southern South America continents to AMS, together with relatively higher local dust availability. The intermediate period from 2.7 to 1.4 cal kyr BP (Fig. 3f), identified by the change-point analysis, is a dust flux transition period characterized by gradual poleward displacement of the SWW.

The timing and strength of the reconstructed environmental changes at AMS from 4.9 to 3.9 cal kyr BP suggest these were part of a larger regional drought event, widely observed around the Indian Ocean. For example, enhanced dry conditions have been found based on the abrupt increased dust deposition in both Kilimanjaro ice cores (~4.0 cal kyr BP, Thompson et al., 2002) and in the Gulf of Oman marine sediment record (4.0 ± 0.1 cal kyr BP, Cullen et al., 2000), based on the positive sea surface salinity in a Northern Red Sea sediment core (~4.2 cal kyr BP, Arz et al., 2006), and based on the reduced annual rainfall evident in the Arabian sea sediment core (~4.2 cal kyr BP, Staubwasser et al., 2003). This mega-drought has potentially led to some of the greatest societal upheavals in historical times (e.g., Egyptian Old Kingdom in the Nile Valley and Akkadian Empire in Mesopotamia, Weiss, 2016). The severe dry conditions are explained by changes in the monsoon system and extra−tropical airflow during winter (e.g., Cullen et al., 2000; Staubwasser et al., 2003), which was suggested to follow variability in solar activity (Cullen et al., 2000; Neff et al., 2001). Weaker SWW at AMS associated with the mega-drought event, suggests a close teleconnection between SWW and other climate features (e.g., monsoon system) in Indian Ocean sector around 4 cal kyr BP.

We compare the AMS dust deposition record to other SH paleoclimate records from different longitudes at the northern edge of SWW (33−41°S, Fig. 6). We find that the AMS dust flux (Fig. 6d) broadly anti-correlates with magnetic susceptibility in an oceanic minerotrophic peat core from Nightingale Island (37°S, Fig. 6e, Lindvall et al., 2011). Magnetic susceptibility is a proxy for surface runoff to this peat mire and therefore tracks rainfall in a very different manner to our dust deposition proxy in the ombrotrophic AMS peat core (for explanations on trophic status see supplementary Text S4). Both AMS and Nightingale cores suggest that the SWW moved poleward at 4.9−3.9 cal kyr BP, and equatorward at

6.2−4.9 cal kyr BP and 3.9−2.7 cal kyr BP. Other published proxy records do not show coherent trends with these two SWW proxy records over the past 6.6 kyr. For example, AMS dust flux, Nightingale Island magnetic susceptibility and Southern Chile pollen composition (Moreno et al., 2010), indicate a poleward shift in SWW from 4.9 to 3.9 cal kyr BP (Fig. 6a, d, e), where other records show no trend (Fig. 6c, g, h), or an equatorward shift in SWW (Fig. 6b, f). Subsequently, during 3.9−2.7 cal kyr BP period, the AMS dust flux, Nightingale Island magnetic susceptibility (Lindvall et al., 2011), Southern Chilean marine iron (Lamy et al., 2001), Central Chilean precipitation (Jenny et al., 2003), and South African nitrogen isotope records (Chase et al., 2013) (Fig. 6d, e, b, g, h, respectively), suggest an equatorward shift in SWW. Conversely the Chilean pollen (Moreno et al., 2010), Western South Atlantic Oxygen isotope (Voigt et al., 2015) and Southeast Australian westerly positon records (Marx et al., 2011) (Fig. 6a, c, f), show no change in SWW from 3.9 to 2.7 cal kyr BP. We speculate that the reasons for the observed variability in SWW proxy records are, 1/the dependence of SWW proxies on complex regional climate factors, and 2/ uncertainty in interpreting these paleo-records due to dating uncertainties, and resolution and inherent complexity of proxies used. A limitation of the AMS peat record is that it does not extend to the late glacial period, where stronger trends in climate proxies have been previously detected (e.g., Kuhnt et al., 2015; Lamy et al., 2010, see Fig. S8). The variations in SWW in the last 6.6 kyr that we infer from the AMS dust record should therefore be regarded as moderate changes, compared to the oscillations in SWW that have been associated with glacial/inter-glacial periods (e.g., De Deckker et al., 2012; Van der Putten et al., 2015). Essentially, the ensemble of paleo-climate records shown in Fig. 6, suggests that SWW are not homogeneous across at its northern zone (33−41°S) over the last 6.6 kyr. More well-dated Holocene records using multiple proxies, and advanced Earth system climate models are needed to understand the geographical variability in SWW dynamics.

4.5. Climatic and anthropogenic influences in the last 100 years

The last 100 years (1910−2014 AD) display distinct REE and ϵNd signatures compared to the rest of the core (Fig. 5; Fig. S9). This is accompanied by a quantitative increase in dust deposition from Southern Africa (Fig. 7). The overall dust flux, however, is not significantly different during the last 100 years compared to the

1.4 cal kyr BP to present and 4.9−3.9 cal kyr BP periods, both characterized by relatively high dust flux and poleward position of the SWW. We therefore suggest that other factors than the position of the SWW play a role in the recent shift in dust provenance from Southern Africa. There is evidence of recent anthropogenic disturbances in the Southern part of the African continent. For example, there is a major shift from grass-dominated to sedge-dominated vegetation in the Okavango Delta (Northern Botswana) due to grazing and fires (Nash et al., 2006). Remote sensing also clearly shows the effects of land clearing, agriculture, and land degradation around Etosha Pan in Namibia (Strain and Engle, 1996). Land degradation in recent years is also found in South Africa (Hoffman and Todd, 2000). These changes to the local landscape enhance soil availability and erosion, thereby promoting a relative increase of distal dust availability and subsequent inputs aligned along the prevailing winds to AMS. Enhanced South African dust input to AMS during the past 100 years may alternatively be caused by an overall drying trend over the South African continent as a response to human-climate interaction (IPCC, 2007). A general trend towards greater aridity and widespread drought in Southern Africa has indeed been recorded since the 19th century (e.g., Kelso and Vogel, 2007; Nicholson, 2001; Nicholson et al., 2012; Riedel et al., 2012), supporting our findings.

5. Conclusions

Understanding Holocene dust cycling and climate change in the Southern Hemisphere is hampered by a paucity of high-resolution records in some sectors. We provide the first Holocene mineral dust record from an Amsterdam Island peat core in the Southern Indian Ocean. Southern South America and Southern Africa have been found to be the main distal dust sources to AMS. Since 6.6 cal kyr BP ago, except for the last 100 years, the dust inputs from local, Southern South America and Southern Africa remained relatively constant, with the former two as the main dust contributors. We interpret millennial scale shifts in dust deposition rates to be caused by shifts in the SWW at AMS. A comparison of inferred SWW dynamics at AMS to other Southern Hemisphere SWW proxy records at the northern edge of the wind belt shows both similarities and differences, which suggests SWW were not zonally homogeneous from mid to late Holocene (Lamy et al., 2019). In the last 100 years, the dust contribution from Southern Africa doubles, possibly as a result of higher dust availability due to a combination of drier climate and human influence (e.g., over-grazing, agriculture and land degradation). We suggest that anthropogenic activities play an important role in the Southern Hemisphere dust cycle during last 100 years.

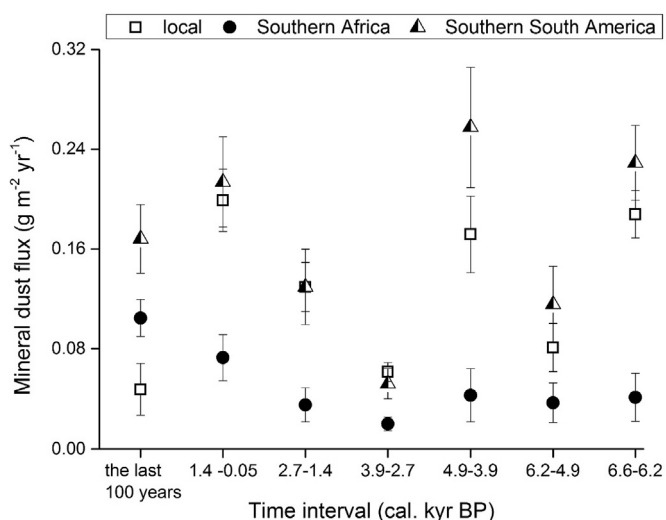**Fig. 7.** The mineral dust contributions of local, Southern Africa and Southern South America (g m^{-2} yr^{-1}, 1σ) during different time intervals.

Appendix A. Supplementary data

Supplementary data to this article can be found online at https://doi.org/10.1016/j.quascirev.2020.106169.

References

Abdi, H., Williams, L.J., 2010. Principal component analysis. Wiley Inter. Rev. Comp. Stat. 2 (4), 433–459. https://doi.org/10.1002/wics.101.

Albarède, F., 1996. Introduction to Geochemical Modeling, 1. paperback ed. (with corr.). ed. Cambridge Univ. Press, Cambridge, p. 34.

Angot, H., Barret, M., Magand, O., Ramonet, M., Dommergue, A., 2014. A 2-year record of atmospheric mercury species at a background Southern Hemisphere station on Amsterdam Island. Atmos. Chem. Phys. 14, 11461–11473. https://doi.org/10.5194/acp-14-11461-2014.

Appleby, P.G., 2001. Chronostratigraphic techniques in recent sediments. In: Last, W.M., Smol, J.P. (Eds.), Tracking Environmental Change Using Lake Sediments. Volume 1: Basin Analysis, Coring, and Chronological Techniques, pp. 171–203.

Arz, H.W., Lamy, F., Pätzold, J., 2006. A pronounced dry event recorded around 4.2 ka in brine sediments from the northern Red Sea. Quat. Res. 66, 432–441. https://doi.org/10.1016/j.yqres.2006.05.006.

Belokopytov, I., Beresnevich, V., 1955. Giktorf's peat borers. Torfyanaya Promyshlennost' 8, 9–10.

Betzer, P.R., Carder, K.L., Duce, R.A., Merrill, J.T., Tindale, N.W., Uematsu, M., Costello, D.K., Young, R.W., Feely, R.A., Breland, J.A., Bernstein, R.E., Greco, A.M., 1988. Long–range transport of giant mineral aerosol particles. Nature 336, 568–571. https://doi.org/10.1038/336568a0.

Blaauw, M., Christen, J.A., 2011. Flexible paleoclimate age-depth models using an autoregressive gamma process. Bayesian Anal 6, 457–474. https://doi.org/10.1214/11-BA618.

Bryant, R.G., Bigg, G.R., Mahowald, N.M., Eckardt, F.D., Ross, S.G., 2007. Dust emission response to climate in southern Africa. J. Geophys. Res. 112, D09207. https://doi.org/10.1029/2005JD007025.

Castino, F., Bookhagen, B., Strecker, M.R., 2016. River-discharge dynamics in the southern central Andes and the 1976-77 global climate shift: discharge dynamics in the central Andes. Geophys. Res. Lett. 43 (11) https://doi.org/10.1002/2016GL070868, 679-11,687.

Chase, B.M., Boom, A., Carr, A.S., Meadows, M.E., Reimer, P.J., 2013. Holocene climate change in southernmost South Africa: rock hyrax middens record shifts in the southern westerlies. Quat. Sci. Rev. 82, 199–205. https://doi.org/10.1016/j.quascirev.2013.10.018.

Chase, B.M., Chevalier, M., Boom, A., Carr, A.S., 2017. The dynamic relationship between temperate and tropical circulation systems across South Africa since the last glacial maximum. Quat. Sci. Rev. 174, 54–62. https://doi.org/10.1016/j.quascirev.2017.08.011.

Chevalier, M., Chase, B.M., 2015. Southeast African records reveal a coherent shift from high- to low-latitude forcing mechanisms along the east African margin across last glacial–interglacial transition. Quat. Sci. Rev. 125, 117–130. https://doi.org/10.1016/j.quascirev.2015.07.009.

Cohen, A.L., Tyson, P.D., 1995. Sea-surface temperature fluctuations during the Holocene off the south coast of Africa: implications for terrestrial climate and rainfall. Holocene 5, 304–312. https://doi.org/10.1177/095968369500500305.

Cordova, C.E., Scott, L., Chase, B.M., Chevalier, M., 2017. Late pleistocene-holocene vegetation and climate change in the middle kalahari, lake Ngami, Botswana. Quat. Sci. Rev. 171, 199–215. https://doi.org/10.1016/j.quascirev.2017.06.036.

Cullen, H.M., deMenocal, P.B., Hemming, S., Hemming, G., Brown, F.H., Guilderson, T., Sirocko, F., 2000. Climate change and the collapse of the Akkadian empire: evidence from the deep sea. Geology 28 (4), 379–382.

Damman, A.W.H., 1978. Distribution and movement of elements in ombrotrophic peat bogs. Oikos 30, 480. https://doi.org/10.2307/3543344.

De Deckker, P., Moros, M., Perner, K., Jansen, E., 2012. Influence of the tropics and southern westerlies on glacial interhemispheric asymmetry. Nat. Geosci. 5, 266–269. https://doi.org/10.1038/ngeo1431.

De Vleeschouwer, F., Chambers, F.M., Swindles, G.T., 2010. Coring and sub-sampling of peatlands for palaeoenvironmental research. Mires Peat 7.

De Vleeschouwer, F., Vanneste, H., Mauquoy, D., Piotrowska, N., Torréjon, F., Roland, T., Stein, A., Le Roux, G., 2014. Emissions from pre-hispanic metallurgy in The south American atmosphere. PLoS One 9, e111315. https://doi.org/10.1371/journal.pone.0111315.

Delqué-Količ, E., Caffy, I., Comby-Zerbino, C., Dumoulin, J.P., Hain, S., Massault, M., Moreau, C., Quiles, A., Setti, V., Souprayen, C., Tannau, J.F., Thellier, B., Vincent, J., 2013. Advances in handling small radiocarbon samples at the laboratoire de Mesure du Carbone 14 in Saclay, France. Radiocarbon 55, 648–656. https://doi.org/10.1017/S0033822200057805.

Denton, G.H., Anderson, R.F., Toggweiler, J.R., Edwards, R.L., Schaefer, J.M., Putnam, A.E., 2010. The last glacial termination. Science 328, 1652–1656. https://doi.org/10.1126/science.1184119.

Doucet, J., Giret, A., Weis, D., Scoates, J., 2003. Géologie des îles Amsterdam et Saint Paul. GEOLOGUES-PARIS, pp. 10–14.

Engelstaedter, S., Washington, R., 2007. Temporal controls on global dust emissions: the role of surface gustiness: temporal controls. Geophys. Res. Lett. 34 https://doi.org/10.1029/2007GL029971.

Fitchett, J.M., Mackay, A.W., Grab, S.W., Bamford, M.K., 2017. Holocene climatic variability indicated by a multi-proxy record from southern Africa's highest wetland. Holocene 27, 638–650. https://doi.org/10.1177/0959683616670467.

Flatberg, I., Whinam, J., Lebouvier, M., 2011. Three species of Sphagnum endemic to Île Amsterdam, Terres Australes et Antarctiques Françaises: S. cavernulosum sp. nov., S. complanatum sp. nov. and S. islei. J. Bryol. 33, 105–121. https://doi.org/10.1179/1743282010Y.0000000019.

Fletcher, M.-S., Moreno, P.I., 2012. Have the Southern Westerlies changed in a zonally symmetric manner over the last 14,000 years? A hemisphere-wide take on a controversial problem. Quat. Int. 253, 32–46. https://doi.org/10.1016/j.quaint.2011.04.042.

Frenot, Y., Valleix, T., 1990. Carte des sols de l'Ile Amsterdam (Terres Australes et Antarctiques Françaises). Université, Station Biologique de Paimpont.

Frölicher, T.L., Sarmiento, J.L., Paynter, D.J., Dunne, J.P., Krasting, J.P., Winton, M., 2015. Dominance of the Southern Ocean in anthropogenic carbon and heat uptake in CMIP5 models. J. Clim. 28, 862–886. https://doi.org/10.1175/JCLI-D-14-00117.1.

Frugone-Álvarez, M., Latorre, C., Giralt, S., Polanco-Martínez, J., Bernárdez, P., Oliva-Urcia, B., Maldonado, A., Carrevedo, M.L., Moreno, A., Delgado Huertas, A., Prego, R., Barreiro-Lostres, F., Valero-Garcés, B., 2017. A 7000-year high-resolution lake sediment record from coastal central Chile (Lago Vichuquén, 34°S): implications for past sea level and environmental variability: high-resolution lake sediment record from CENTRAL Chile. J. Quat. Sci. 32, 830–844. https://doi.org/10.1002/jqs.2936.

Gaiero, D., 2007. Dust provenance in Antarctic ice during glacial periods: from where in southern South America? Geophys. Res. Lett. 34, L17707. https://doi.org/10.1029/2007GL030520.

Gaiero, D.M., Simonella, L., Gassó, S., Gili, S., Stein, A.F., Sosa, P., Becchio, R., Arce, J., Marelli, H., 2013. Ground/satellite observations and atmospheric modeling of dust storms originating in the high Puna-Altiplano deserts (South America): implications for the interpretation of paleo-climatic archives: dust storms from puna-altiplano deserts. J. Geophys. Res. Atmos. 118, 3817–3831. https://doi.org/10.1002/jgrd.50036.

Gaudichet, A., Lefèvre, R., Gaudry, A., Ardouin, B., Lambert, G., Miller, J.M., 1989. Mineralogical composition of aerosols at Amsterdam island. Tellus B 41B, 344–352. https://doi.org/10.1111/j.1600-0889.1989.tb00313.x.

Gili, S., Gaiero, D.M., Goldstein, S.L., Chemale, F., Jweda, J., Kaplan, M.R., Becchio, R.A., Koester, E., 2017. Glacial/interglacial changes of Southern Hemisphere wind circulation from the geochemistry of South American dust. Earth Planet. Sci. Lett. 469, 98–109. https://doi.org/10.1016/j.epsl.2017.04.007.

Gillett, N.P., Thompson, D.W., 2003. Simulation of recent Southern Hemisphere climate change. Science 302 (5643), 273–275. https://doi.org/10.1126/science.1087440.

Givelet, N., Le Roux, G., Cheburkin, A., Chen, B., Frank, J., Goodsite, M.E., Kempter, H., Krachler, M., Noernberg, T., Rausch, N., Rheinberger, S., Roos-Barraclough, F., Sapkota, A., Scholz, C., Shotyk, W., 2004. Suggested protocol for collecting, handling and preparing peat cores and peat samples for physical, chemical, mineralogical and isotopic analyses. J. Environ. Monit. 6, 481–492. https://doi.org/10.1039/B401601G.

Goodsite, M.E., Rom, W., Heinemeier, J., Lange, T., Ooi, S., Appleby, P.G., Shotyk, W., van der Knaap, W.O., Lohse, C., Hansen, T.S., 2001. High-resolution AMS 14 C dating of post-bomb peat archives of atmospheric pollutants. Radiocarbon 43, 495–515. https://doi.org/10.1017/S0033822200041163.

Hande, L.B., Siems, S.T., Manton, M.J., 2012. Observed trends in wind speed over the Southern Ocean: southern OCEAN wind trends. Geophys. Res. Lett. 39, n/a-n/a. https://doi.org/10.1029/2012GL051734.

Hodgson, D.A., Sime, L.C., 2010. Southern westerlies and CO2. Nat. Geosci. 3, 666–667. https://doi.org/10.1038/ngeo970.

Hoffman, M.T., Todd, T., 2000. A national review of land degradation in South Africa: the influence of biophysical and socio-economic factors. J. South. Afr. Stud. 26 (4), 743–758.

Hogg, A.G., Hua, Q., Blackwell, P.G., Niu, M., Buck, C.E., Guilderson, T.P., Heaton, T.J.,

Palmer, J.G., Reimer, P.J., Reimer, R.W., Turney, C.S.M., Zimmerman, S.R.H., 2013. SHCal13 southern hemisphere calibration, 0–50,000 Years cal BP. Radiocarbon 55, 1889–1903. https://doi.org/10.2458/azu_js_rc.55.16783.

Hua, Q., 2009. Radiocarbon: a chronological tool for the recent past. Quat. Geochronol. 4, 378–390. https://doi.org/10.1016/j.quageo.2009.03.006.

Hua, Q., Barbetti, M., Rakowski, A.Z., 2013. Atmospheric radiocarbon for the period 1950–2010. Radiocarbon 55 (4), 2059–2072. https://doi.org/10.2458/azu_js_rc.v55i2.16177.

Humphries, M.S., Benitez-Nelson, C.R., Bizimis, M., Finch, J.M., 2017. An aeolian sediment reconstruction of regional wind intensity and links to larger scale climate variability since the last deglaciation from the east coast of southern Africa. Glob. Planet. Chang. 156, 59–67. https://doi.org/10.1016/j.gloplacha.2017.08.002.

Jacobsen, S.B., Wasserburg, G.J., 1980. Sm-Nd isotopic evolution of chondrites. Earth Planet. Sci. Lett. 50, 139–155. https://doi.org/10.1016/0012-821X(80)90125-9.

Jenny, B., Wilhelm, D., Valero-Garcés, B., 2003. The Southern Westerlies in Central Chile: holocene precipitation estimates based on a water balance model for Laguna Aculeo (33°50′S). Clim. Dyn. 20, 269–280. https://doi.org/10.1007/s00382-002-0267-3.

Johnson, M.S., Meskhidze, N., Kiliyanpilakkil, V.P., Gassó, S., 2011. Understanding the transport of Patagonian dust and its influence on marine biological activity in the South Atlantic Ocean. Atmos. Chem. Phys. 11, 2487–2502. https://doi.org/10.5194/acp-11-2487-2011.

Kelso, C., Vogel, C., 2007. The climate of Namaqualand in the nineteenth century. Clim. Change 83, 357–380. https://doi.org/10.1007/s10584-007-9264-1.

Kienast, S.S., Winckler, G., Lippold, J., Albani, S., Mahowald, N.M., 2016. Tracing dust input to the global ocean using thorium isotopes in marine sediments: ThoroMap: ThoroMap. Glob. Biogeochem. Cycles 30, 1526–1541. https://doi.org/10.1002/2016GB005408.

Killick, R., Eckley, I.A., Ewans, K., Jonathan, P., 2010. Detection of changes in variance of oceanographic time-series using changepoint analysis. Ocean. Eng. 37, 1120–1126. https://doi.org/10.1016/j.oceaneng.2010.04.009.

Kohfeld, K.E., Graham, R.M., de Boer, A.M., Sime, L.C., Wolff, E.W., Le Quéré, C., Bopp, L., 2013. Southern Hemisphere westerly wind changes during the Last Glacial Maximum: paleo-data synthesis. Quat. Sci. Rev. 68, 76–95. https://doi.org/10.1016/j.quascirev.2013.01.017.

Kuhnt, W., Holbourn, A., Xu, J., Opdyke, B., De Deckker, P., Röhl, U., Mudelsee, M., 2015. Southern Hemisphere control on Australian monsoon variability during the late deglaciation and Holocene. Nat. Commun. 6, 5916. https://doi.org/10.1038/ncomms6916.

Lamy, F., Chiang, J.C.H., Martínez-Méndez, G., Thierens, M., Arz, H.W., Bosmans, J., Hebbeln, D., Lambert, F., Lembke-Jene, L., Stuut, J.-B., 2019. Precession modulation of the South Pacific westerly wind belt over the past million years. Proc. Natl. Acad. Sci. U.S.A. 116, 23455–23460. https://doi.org/10.1073/pnas.1905847116.

Lamy, F., Hebbeln, D., Röhl, U., Wefer, G., 2001. Holocene rainfall variability in southern Chile: a marine record of latitudinal shifts of the Southern Westerlies. Earth Planet. Sci. Lett. 185, 369–382. https://doi.org/10.1016/S0012-821X(00)00381-2.

Lamy, F., Kilian, R., Arz, H.W., Francois, J.-P., Kaiser, J., Prange, M., Steinke, T., 2010. Holocene changes in the position and intensity of the southern westerly wind belt. Nat. Geosci. 3, 695–699. https://doi.org/10.1038/ngeo959.

Landschützer, P., Gruber, N., Haumann, F.A., Rödenbeck, C., Bakker, D.C.E., van Heuven, S., Hoppema, M., Metzl, N., Sweeney, C., Takahashi, T., Tilbrook, B., Wanninkhof, R., 2015. The reinvigoration of the Southern Ocean carbon sink. Science 349, 1221–1224. https://doi.org/10.1126/science.aab2620.

Lebouvier, M., Frenot, Y., 2007. And Île Saint-Paul temperate. All have endemic species amongst their biota. The Terres Australes et Antarctiques Françaises (TAAF) is. In: Papers and Proceedings of the Royal Society of Tasmania, vol. 141. Royal Society of Tasmania, p. 23. No. 1.

Li, C., Le Roux, G., Sonke, J., van Beek, P., Souhaut, M., Van der Putten, N., De Vleeschouwer, F., 2017. Recent 210 Pb, 137 Cs and 241 Am accumulation in an ombrotrophic peatland from Amsterdam island (southern Indian ocean). J. Environ. Radioact. 175–176, 164–169. https://doi.org/10.1016/j.jenvrad.2017.05.004.

Li, F., Ginoux, P., Ramaswamy, V., 2008. Distribution, transport, and deposition of mineral dust in the Southern Ocean and Antarctica: contribution of major sources. J. Geophys. Res. 113, D10207. https://doi.org/10.1029/2007JD009190.

Lindvall, H., Björck, S., Holmgren, S., Ljung, K., Van der Putten, N., Porter, C., 2011. A Holocene peat record in the central South Atlantic: an archive of precipitation changes. GFF 133, 195–206. https://doi.org/10.1080/11035897.2011.633708.

Ljung, K., Björck, S., 2007. Holocene climate and vegetation dynamics on Nightingale Island, South Atlantic—an apparent interglacial bipolar seesaw in action? Quat. Sci. Rev. 26, 3150–3166. https://doi.org/10.1016/j.quascirev.2007.08.003.

Lovenduski, N.S., Gruber, N., Doney, S.C., 2008. Toward a mechanistic understanding of the decadal trends in the Southern Ocean carbon sink: southern OCEAN CO 2 flux trends. Glob. Biogeochem. Cycles 22. https://doi.org/10.1029/2007GB003139 n/a-n/a.

Mahowald, N.M., Baker, A.R., Bergametti, G., Brooks, N., Duce, R.A., Jickells, T.D., Kubilay, N., Prospero, J.M., Tegen, I., 2005. Atmospheric global dust cycle and iron inputs to the ocean: atmospheric iron deposition. Glob. Biogeochem. Cycles 19. https://doi.org/10.1029/2004GB002402 n/a-n/a.

Marshall, G.J., Orr, A., van Lipzig, N.P.M., King, J.C., 2006. The impact of a changing southern hemisphere annular Mode on antarctic peninsula summer temperatures. J. Clim. 19, 5388–5404. https://doi.org/10.1175/JCLI3844.1.

Marx, S.K., Kamber, B.S., McGowan, H.A., Denholm, J., 2011. Holocene dust deposition rates in Australia's Murray-Darling Basin record the interplay between aridity and the position of the mid-latitude westerlies. Quat. Sci. Rev. 30, 3290–3305. https://doi.org/10.1016/j.quascirev.2011.07.015.

Marx, S.K., Kamber, B.S., McGowan, H.A., Petherick, L.M., McTainsh, G.H., Stromsoe, N., Hooper, J.N., May, J.-H., 2018. Palaeo-dust records: a window to understanding past environments. Glob. Planet. Chang. 165, 13–43. https://doi.org/10.1016/j.gloplacha.2018.03.001.

Marx, S.K., McGowan, H.A., Kamber, B.S., 2009. Long-range dust transport from eastern Australia: a proxy for Holocene aridity and ENSO-type climate variability. Earth Planet. Sci. Lett. 282, 167–177. https://doi.org/10.1016/j.epsl.2009.03.013.

Miller, J.M., Moody, J.L., Harris, J.M., Gaudry, A., 1993. A 10-year trajectory flow climatology for Amsterdam Island, 1980–1989. Atmospheric Environment. Part A. General Topics 27. https://doi.org/10.1016/0960-1686(93)90296-B, 1909–1916.

Moody, J.L., Pszenny, A.A.P., Gaudry, A., Keene, W.C., Galloway, J.N., Polian, G., 1991. Precipitation composition and its variability in the southern Indian ocean: Amsterdam island, 1980–1987. J. Geophys. Res. 96, 20769. https://doi.org/10.1029/91JD01921.

Moreau, C., Caffy, I., Comby, C., Delqué-Količ, E., Dumoulin, J.-P., Hain, S., Quiles, A., Setti, V., Souprayen, C., Thellier, B., Vincent, J., 2013. Research and development of the Artemis 14 C AMS facility: status report. Radiocarbon 55, 331–337. https://doi.org/10.1017/S0033822200057441.

Moreno, P.I., Francois, J.P., Moy, C.M., Villa-Martínez, R., 2010. Covariability of the southern westerlies and atmospheric CO2 during the holocene. Geology 38, 727–730. https://doi.org/10.1130/G30962.1.

Nash, D.J., Meadows, M.E., Gulliver, V.L., 2006. Holocene environmental change in the Okavango Panhandle, northwest Botswana. Quat. Sci. Rev. 25, 1302–1322. https://doi.org/10.1016/j.quascirev.2005.11.004.

Neff, U., Burns, S.J., Mangini, A., Mudelsee, M., Fleitmann, D., Matter, A., 2001. Strong coherence between solar variability and the monsoon in Oman between 9 and 6 kyr ago. Nature 411 (6835), 290. https://doi.org/10.1038/35077048.

Nicholson, S., 2001. Climatic and environmental change in Africa during the last two centuries. Clim. Res. 17, 123–144. https://doi.org/10.3354/cr017123.

Nicholson, S.E., Dezfuli, A.K., Klotter, D., 2012. A two-century precipitation dataset for the continent of Africa. Bull. Am. Meteorol. Soc. 93, 1219–1231. https://doi.org/10.1175/BAMS-D-11-00212.1.

Orsi, A.H., Whitworth, T., Nowlin, W.D., 1995. On the meridional extent and fronts of the Antarctic Circumpolar Current. Deep Sea Res. Oceanogr. Res. Pap. 42, 641–673. https://doi.org/10.1016/0967-0637(95)00021-W.

IPCC, 2007. In: Parry, M.L. (Ed.), Climate Change 2007 - Impacts, Adaptation and Vulnerability: Contribution of Working Group II to the Fourth Assessment Report of the Intergovernmental Panel on Climate Change, vol. 1. publ. ed. Cambridge Univ. Press, Cambridge.

Piketh, S.J., 2002. Chemical evidence of long-range atmospheric transport over southern Africa. J. Geophys. Res. 107, 4817. https://doi.org/10.1029/2002JD002056.

Piotrowska, N., 2013. Status report of AMS sample preparation laboratory at GADAM Centre, Gliwice, Poland. Nucl. Instrum. Methods Phys. Res. Sect. B Beam Interact. Mater. Atoms 294, 176–181. https://doi.org/10.1016/j.nimb.2012.05.017.

Polian, G., Lambert, G., Ardouin, B., Jegou, A., 1986. Long-range transport of continental radon in subantarctic and antarctic areas. Tellus B Chem. Phys. Meteorol. 38, 178–189. https://doi.org/10.3402/tellusb.v38i3-4.15126.

Prospero, J.M., Ginoux, P., Torres, O., Nicholson, S.E., Gill, T.E., 2002. Environmental characterization of global sources of atmospheric soil dust identified with the NIMBUS 7 Total Ozone Mapping Spectrometer (TOMS) absorbing aerosol product. Rev. Geophys. 40, 1002. https://doi.org/10.1029/2000RG000095.

Pueyo, J.J., Sáez, A., Giralt, S., Valero-Garcés, B.L., Moreno, A., Bao, R., Schwalb, A., Herrera, C., Klosowska, B., Taberner, C., 2011. Carbonate and organic matter sedimentation and isotopic signatures in Lake Chungará, Chilean Altiplano, during the last 12.3kyr. Palaeogeogr. Palaeoclimatol. Palaeoecol. 307, 339–355. https://doi.org/10.1016/j.palaeo.2011.05.036.

R Development Core Team, 2013. R: A Language and Environment for Statistical Computing. R version 3.0.0. R Foundation for Statistical Computing, Vienna, Austria.

Reid, P.C., Hari, R.E., Beaugrand, G., Livingstone, D.M., Marty, C., Straile, D., Barichivich, J., Goberville, E., Adrian, R., Aono, Y., Brown, R., Foster, J., Groisman, P., Hélaouët, P., Hsu, H.-H., Kirby, R., Knight, J., Kraberg, A., Li, J., Lo, T.-T., Myneni, R.B., North, R.P., Pounds, J.A., Sparks, T., Stübi, R., Tian, Y., Wiltshire, K.H., Xiao, D., Zhu, Z., 2016. Global impacts of the 1980s regime shift. Glob. Chang. Biol. 22, 682–703. https://doi.org/10.1111/gcb.13106.

Revelle, 2019. Procedures for Psychological, Psychometric, and Personality Research. https://personality-project.org/r/psych/.

Riedel, F., Erhardt, S., Chauke, C., Kossler, A., Shemang, E., Tarasov, P., 2012. Evidence for a permanent lake in Sua Pan (Kalahari, Botswana) during the early centuries of the last millennium indicated by distribution of Baobab trees (Adansonia digitata) on "Kubu Island". Quat. Int. 253, 67–73. https://doi.org/10.1016/j.quaint.2011.02.040.

Sabine, C.L., Feely, R.A., Gruber, N., Key, R.M., Lee, K., Bullister, J.L., Wanninkhof, R., Wong, C.S.L., Wallace, D.W., Tilbrook, B., Millero, F.J., 2004. The oceanic sink for anthropogenic CO2. Science 305, 367–371. https://doi.org/10.1126/science.1097403.

Saunders, K.M., Kamenik, C., Hodgson, D.A., Hunziker, S., Siffert, L., Fischer, D., Fujak, M., Gibson, J.A.E., Grosjean, M., 2012. Late Holocene changes in

precipitation in northwest Tasmania and their potential links to shifts in the Southern Hemisphere westerly winds. Glob. Planet. Chang. 92 (93), 82–91. https://doi.org/10.1016/j.gloplacha.2012.04.005.

Saunders, K.M., Roberts, S.J., Perren, B., Butz, C., Sime, L., Davies, S., Van Nieuwenhuyze, W., Grosjean, M., Hodgson, D.A., 2018. Holocene dynamics of the Southern Hemisphere westerly winds and possible links to CO2 outgassing. Nat. Geosci. 11, 650–655. https://doi.org/10.1038/s41561-018-0186-5.

Shotyk, W., 1997. Atmospheric deposition and mass balance of major and trace elements in two oceanic peat bog profiles, northern Scotland and the Shetland Islands. Chem. Geol. 138, 55–72. https://doi.org/10.1016/S0009-2541(96)00172-6.

Shulmeister, J., 1999. Australasian evidence for mid-holocene climate change implies precessional control of Walker Circulation in the Pacific. Quat. Int. 57 (58), 81–91. https://doi.org/10.1016/S1040-6182(98)00052-4.

Spalding, K.L., Buchholz, B.A., Bergman, L.E., Druid, H., Frisén, J., 2005. Forensics: age written in teeth by nuclear tests. Nature 437 (7057), 333. https://doi.org/10.1038/437333a.

Staubwasser, M., Sirocko, F., Grootes, P.M., Segl, M., 2003. Climate change at the 4.2 ka BP termination of the Indus valley civilization and Holocene south Asian monsoon variability: south asian holocene climate change. Geophys. Res. Lett. 30 https://doi.org/10.1029/2002GL016822.

Strain, P., Engle, F., 1996. Looking at Earth. Turner, Atlanta, Ga, p. pp304.

Swart, N.C., Fyfe, J.C., 2012. Observed and simulated changes in the Southern Hemisphere surface westerly wind-stress. Geophys. Res. Lett. 39 (16) https://doi.org/10.1029/2012GL052810.

Taylor, W., 2000a. Change-Point Analyzer 2.3 Shareware Program. Taylor Enterprises, Libertyville, Illinois. Retrieved from. http://www.variation.com/cpa/.

Taylor, W., 2000b. Change-Point Analysis: A Powerful New Tool for Detecting Changes. Retrieved from. http://www.variation.com/cpa/tech/changepoint.html.

Thompson, D.W.J., Solomon, S., 2002. Interpretation of recent southern hemisphere climate change. Science 296, 895–899. https://doi.org/10.1126/science.1069270.

Thompson, L.G., Mosley-Thompson, E., Davis, M.E., Henderson, K.A., Brecher, H.H., Zagorodnov, V.S., Mashiotta, T.A., Lin, P.-N., Mikhalenko, V.N., Hardy, D.R., 2002. Kilimanjaro ice core records: evidence of holocene climate change in tropical Africa. Science 298, 589–593. https://doi.org/10.1126/science.1073198.

Van der Putten, N., Hébrard, J.-P., Verbruggen, C., Van de Vijver, B., Disnar, J.-R., Spassov, S., de Beaulieu, J.-L., De Dapper, M., Keravis, D., Hus, J., Thouveny, N., Frenot, Y., 2008. An integrated palaeoenvironmental investigation of a 6200 year old peat sequence from Ile de la Possession, Iles Crozet, sub-Antarctica. Palaeogeogr. Palaeoclimatol. Palaeoecol. 270, 179–195. https://doi.org/10.1016/j.palaeo.2008.09.014.

Van der Putten, N., Mauquoy, D., Verbruggen, C., Björck, S., 2012. Subantarctic peatlands and their potential as palaeoenvironmental and palaeoclimatic archives. Quat. Int. 268, 65–76. https://doi.org/10.1016/j.quaint.2011.07.032.

Van der Putten, N., Verbruggen, C., Björck, S., Michel, E., Disnar, J.-R., Chapron, E., Moine, B.N., de Beaulieu, J.-L., 2015. The last termination in The south Indian ocean: a unique terrestrial record from kerguelen islands (49°S) situated within the Southern hemisphere westerly belt. Quat. Sci. Rev. 122, 142–157. https://doi.org/10.1016/j.quascirev.2015.05.010.

Vanneste, H., De Vleeschouwer, F., Bertrand, S., Martínez-Cortizas, A., Vanderstraeten, A., Mattielli, N., Coronato, A., Piotrowska, N., Jeandel, C., Roux, G.L., 2016. Elevated dust deposition in Tierra del Fuego (Chile) resulting from Neoglacial Darwin Cordillera glacier fluctuations: NEOGLACIAL elevated dust deposition IN TIERRA del FUEGO. J. Quat. Sci. 31, 713–722. https://doi.org/10.1002/jqs.2896.

Vanneste, H., De Vleeschouwer, F., Martínez-Cortizas, A., von Scheffer, C., Piotrowska, N., Coronato, A., Le Roux, G., 2015. Late-glacial elevated dust deposition linked to westerly wind shifts in southern South America. Sci. Rep. 5, 11670. https://doi.org/10.1038/srep11670.

Varma, V., Prange, M., Lamy, F., Merkel, U., Schulz, M., 2011. Solar-forced shifts of the southern westerlies during the holocene. Clim. Past 7, 339–347. https://doi.org/10.5194/cp-7-339-2011.

Varma, V., Prange, M., Merkel, U., Kleinen, T., Lohmann, G., Pfeiffer, M., Renssen, H., Wagner, A., Wagner, S., Schulz, M., 2012. Holocene evolution of the Southern Hemisphere westerly winds in transient simulations with global climate models. Clim. Past 8, 391–402. https://doi.org/10.5194/cp-8-391-2012.

Vickery, K.J., Eckardt, F.D., Bryant, R.G., 2013. A sub-basin scale dust plume source frequency inventory for southern Africa, 2005–2008. Geophys. Res. Lett. 40, 5274–5279. https://doi.org/10.1002/grl.50968.

Voigt, I., Chiessi, C.M., Prange, M., Mulitza, S., Groeneveld, J., Varma, V., Henrich, R., 2015. Holocene shifts of the southern westerlies across The south atlantic: holocene shifts of southern westerlies. Paleoceanography 30, 39–51. https://doi.org/10.1002/2014PA002677.

Von Holdt, J.R., Eckardt, F.D., Wiggs, G.F.S., 2017. Landsat identifies aeolian dust emission dynamics at the landform scale. Remote Sens. Environ. 198, 229–243. https://doi.org/10.1016/j.rse.2017.06.010.

Wedepohl, K.H., 1995. The composition of the continental crust. Geochem. Cosmochim. Acta 59 (7), 1217–1232.

Weiss, H., 2016. Global megadrought, societal collapse and resilience at 4.2-3.9 ka BP across the Mediterranean and west Asia. PAGES Mag 24, 62–63. https://doi.org/10.22498/pages.24.2.62.

Zickfeld, K., Fyfe, J.C., Saenko, O.A., Eby, M., Weaver, A.J., 2007. Response of the global carbon cycle to human-induced changes in Southern Hemisphere winds. Geophys. Res. Lett. 34, L12712. https://doi.org/10.1029/2006GL028797.